Modeling of diamagnetic stabilization of ideal magnetohydrodynamic instabilities associated with the transport barrier

G. T. A. Huysmans
Association EURATOM–CEA Cadarache, 13108 St. Paul-Lez-Durance, France

S. E. Sharapov
EURATOM/UKAEA Fusion Association, Culham Science Centre, Abingdon, OXON OX14 3EA, United Kingdom

A. B. Mikhailovskii
Institute for Nuclear Fusion, RRC Kurchatov Institute, Kurchatov Sqr. 1, Moscow 123182, Russia

W. Kerner
European Commission, D.G. XII, Square de Meeus 8, Brussels, Belgium

A new code, MISHKA-D (Drift MHD), has been developed as an extension of the ideal magnetohydrodynamics (MHD) code MISHKA-1 in order to investigate the finite gyroradius stabilizing effect of ion diamagnetic drift frequency, ω_{*i}, on linear ideal MHD eigenmodes in tokamaks in general toroidal geometry. The MISHKA-D code gives a self-consistent computation of both stable and unstable eigenmodes with eigenvalues $|\gamma| \cong \omega_{*i}$ in plasmas with strong radial variation in the ion diamagnetic frequency. Test results of the MISHKA-D code show good agreement with the analytically obtained ω_{*i} spectrum and stability limits of the internal kink mode, $n/m = 1/1$, used as a benchmark case. Finite-n ballooning and low-n kink (peeling) modes in the edge transport barrier just inside the separatrix are studied for high confinement mode (H-mode) plasmas with the ω_{*i} effect included. The ion diamagnetic stabilization of the ballooning modes is found to be most effective for narrow edge pedestals. For low enough plasma density the ω_{*i} stabilization can lead to a second zone of ballooning stability, in which all the ballooning modes are stable for any value of the pressure gradient. For internal transport barriers typical of the Joint European Torus [JET, P. H. Rebut *et al.*, *Proceedings of the 10th International Conference, Plasma Physics and Controlled Nuclear Fusion, London* (International Atomic Energy Agency, Vienna, 1985), Vol. I, p. 11] optimized shear discharges, the stabilizing influence of ion diamagnetic frequency on the $n = 1$ global pressure driven disruptive mode is studied. A strong radial variation of ω_{*i} is found to significantly decrease the stabilizing ω_{*i} effect on the $n = 1$ mode, in comparison with the case of constant ω_{*i} estimated at the foot of the internal transport barrier. © *2001 American Institute of Physics.* [DOI: 10.1063/1.1398573]

I. INTRODUCTION

Ideal magnetohydrodynamic (MHD) instabilities play an important role in limiting plasma performance in tokamaks. A careful assessment of the stabilizing effects on ideal MHD modes is important for controlling these instabilities and obtaining highest plasma parameters and fusion yield. In order to compute the ideal MHD instabilities the ideal MHD eigenvalue code MISHKA-1 was developed[1] and successfully applied to Joint European Torus (JET[25]) discharges.[2,3] It was established in Refs. 2 and 3 that the effect of MHD instabilities on plasma confinement is most dramatic if the MHD modes are associated with the so-called "transport barriers," which suppress the thermal plasma transport in a narrow region and control the high confinement of the plasma.[4,5] On JET, two broadly different scenarios of high plasma confinement with transport barriers are established: the high confinement mode (H-mode)[4] and the optimized shear scenario.[5]

In an H-mode discharge, a transport barrier is formed at the plasma edge just inside the magnetic separatrix where the density and temperature vary strongly over very short distances of few centimeters. The edge-localized modes (ELMs) of the first type excited in the edge transport barrier lead to a rapid degradation of plasma performance in a region much broader than the edge only, and they are usually the most limiting MHD evens of the plasma performance in H-mode. Studies[2,6–8] of the MHD stability at the plasma edge have identified the ideal ballooning modes[6–8] and low-n kink (peeling) modes[2,6] driven by the pressure gradient at the edge and by the edge currents (including bootstrap current) as the MHD modes, which determine stability of the ELMs.

In the optimized shear scenario,[5] an internal transport barrier is triggered close to the plasma center and expands at later times. Large radial gradients of ion temperature, up to 150 keV/m, and radial gradients of plasma pressure, up to 10^6 Pa/m, were measured in best discharges with internal transport barriers on JET.[5] Such discharges often end with disruptions, which are attributed to a global ideal MHD kink mode with toroidal mode number $n = 1$ driven by the strong

peaking of the pressure profile at the internal transport barrier.[3]

Since the ideal MHD modes in the barriers are associated with large pressure gradients, more comprehensive analysis of the stability margins must take into account all the relevant pressure-dependent effects, which can modify the stability conditions. One of the well-known effects, which can dramatically modify the stability of ideal MHD modes is the finite gyroradius effect of the ion diamagnetic drift frequency, $\omega_{*i} = (m/r) \cdot (T_i/e_i B_0) \cdot (d \ln p_i/dr) \propto (1/p_i) \cdot (dp_i/dr)$, which can stabilize ideal MHD modes if their growth rate γ_{MHD} is comparable to or lower than ω_{*i} (see Refs. 7–9 and references therein):

$$\gamma_{MHD} \lesssim \omega_{*i}. \tag{1}$$

Here T_i, e_i, and p_i are temperature, charge, and pressure of the thermal ions of the plasma, B_0 is the equilibrium magnetic field, r is the radial coordinate, and m is the poloidal mode number. Introducing the characteristic ion pressure-gradient scale $L_p \equiv |d(\ln p_i)/dr|^{-1}$, and representing

$$\gamma_{MHD} = V_{Ti}/R_{eff}, \tag{2}$$

where R_{eff} is an effective curvature radius of the magnetic field lines, one can rewrite (1) in the form

$$nq\frac{\rho_i}{L_p} \geqslant \frac{r}{R_{eff}}, \tag{3}$$

where $\rho_i = V_{Ti}/\omega_{Bi}$ is the ion Larmor radius, $\omega_{Bi} = e_i B_0/M_i$ is the ion cyclotron frequency, $V_{Ti} = (T_i/M_i)^{1/2}$, M_i is the ion mass, n is the toroidal mode number, and $q(r) = rB_T/R_0 B_P$ is the safety factor (R_0 is the major radius of the torus, B_T and B_P are the values of toroidal and poloidal magnetic fields).

One can see from (3) that the efficiency of the ω_{*i} stabilization is determined by different reasons for modes with different characteristic parameters. For example, the ideal MHD internal kink mode,[10] which is characterized by the toroidal and dominant poloidal mode numbers $n/m = 1/1$, can be easily stabilized by the ion diamagnetic drift effect due to the small values of the growth rate. In this case inequality (3) is satisfied due to the very small "effective" curvature in toroidal geometry, which is of the order of

$$\frac{1}{R_{eff}} \lesssim \frac{\varepsilon^2}{R_0}, \tag{4}$$

where $\varepsilon = r/R_0$, $r = r_1$ is the radius of magnetic surface $q(r_1) = 1$. Then (3) reduces to the following estimate of the plasma parameters at which the ion diamagnetic effect becomes important for the internal kink mode:

$$\frac{\rho_i}{L_p} > \frac{\varepsilon^2}{R_0}, \tag{5}$$

where ρ_i and L_p have to be estimated at the position of the inertial layer of the kink mode, i.e., at $q(r_1) = 1$.

In the case of high-n ballooning modes and kink modes with high m, n, the ω_{*i} stabilization plays an important role since the left-hand side of (3) is proportional to a large value n. As an estimate for $1/R_{eff}$, one can use in this case

$$1/R_{eff} \cong \varepsilon/R_0, \tag{6}$$

so that an estimate for maximum n, n_{max}, above which one could expect a stabilization of high-n modes due to the ω_{*i} effect, takes a form

$$n_{max} \cong \frac{\varepsilon^2 L_p}{q\rho_i}. \tag{7}$$

Considering the relevant plasma parameters typical of the edge transport barrier just inside the separatrix in the H-mode and the plasma parameters typical of the internal transport barriers in the shear optimized scenario, one finds that the condition (1) is satisfied in many cases. Thus, generally speaking, the ω_{*i} effect must be taken into account for stability analysis of ideal MHD modes associated with the transport barriers. Recent analyses[7,8] confirm the importance of the ω_{*i} effect on ideal ballooning modes in the edge transport barriers. It was shown in Ref. 7 with the use of Braginskii equations and simple analytical model, that the ion diamagnetic drift and the finite radial localization of the pedestal pressure gradient change significantly the pressure gradient threshold for ideal ballooning modes. Recent analytical study[8] devoted to the stability of ideal ballooning modes in the edge transport barrier, also has underlined the importance of strong radial variation of the ion diamagnetic frequency. In order to incorporate the effect of strong radial variation of ω_{*i}, a global mode analysis was developed for the ballooning approach.[8]

The goal of the present paper is to develop an ion diamagnetic drift modification of the ideal MHD spectral code MISHKA-1.[1] The modified drift MHD code (called MISHKA-D) should allow to compute stable and unstable eigenmodes with eigenvalues $|\gamma| \cong \omega_{*i}$, in full toroidal geometry and with strong radial variation in the ion diamagnetic frequency, ω_{*i}, taken into account. The MISHKA-D model and numerical method of solving the MISHKA-D equations are presented in Secs. II and III, respectively.

The MISHKA-D code is benchmarked against analytical results for the ω_{*i} effect on the $n/m = 1/1$ internal kink mode in Sec. IV. A short description of the analytical results is given. Auxiliary codes based on the MISHKA-D code, i.e., the antenna version of the MISHKA-D and the continuum solver based on the MISHKA-D code, are tested for the internal kink mode.

The main application of the new MISHKA-D code is the analysis of the ω_{*i} stabilization of ballooning and kink (peeling) modes localized in the edge pedestal of H-mode discharges (Sec. V). The MISHKA-D code allows accurate calculations of finite-n ballooning and kink modes up to very large toroidal mode numbers ($n < 50$–100) in full toroidal geometry and for arbitrary plasma shapes. In order to quantify the relevance of the ion-diamagnetic stabilization, a JET high performance H-mode discharge is analyzed.

The ω_{*i} stabilization of the disruptive $n = 1$ pressure-driven mode in optimized shear discharge with internal transport barrier is considered in Sec. VI.

Conclusions are presented in Sec. VII.

II. THE MODEL

A. Starting equations

Starting equations of the MISHKA-D model are, on the one hand, a generalization of the ideal MHD equations used in the MISHKA-1 code,[1] and, on the other hand, a reduced set of the generalized MHD equations.[11] In contrast to Ref. 1, but by analogy with Ref. 11, we take into account the gyro-viscosity term in the equation of the plasma motion across the magnetic field

$$\rho \, d\mathbf{V}/dt = -\nabla p + \mathbf{j} \times \mathbf{B} + \nabla \cdot \overset{\leftrightarrow}{\pi}_\Lambda, \tag{8}$$

where $\overset{\leftrightarrow}{\pi}_\Lambda$ is the gyroviscosity tensor, $d/dt = \partial/\partial t + \mathbf{V} \cdot \nabla$, $\rho = M_i n$, $\mathbf{V}$, p are the plasma mass density, velocity, and pressure, $\mathbf{j}$ is the electric current density, $\mathbf{B}$ is the magnetic field, M_i is the ion mass, n is the plasma number density. We take the time dependence of the perturbations in the form $\exp(\lambda t)$ and linearize (8) taking into account that the gyroviscosity term compensates the part of the term with $d\mathbf{V}/dt$ related to the ion diamagnetic drift velocity in (8) (see Ref. 11 for details). The linearized version of (8) then reduces to (cf. Refs. 1 and 11)

$$\lambda M_i n_0 \widetilde{\mathbf{V}} = -\nabla \widetilde{p} + \widetilde{\mathbf{H}}, \tag{9}$$

where

$$\widetilde{\mathbf{H}} = (\nabla \times \mathbf{B}_0) \times \widetilde{\mathbf{B}} - \mathbf{B}_0 \times (\nabla \times \widetilde{\mathbf{B}}), \tag{10}$$

the subscript zero and tilde denote the equilibrium and perturbed values. We only consider projections of (9) perpendicular with respect to the equilibrium magnetic field, since only these projections are important for our problem.

The linearized perpendicular Ohm's law is taken allowing for the ion pressure gradient and the equilibrium diamagnetic drift velocity $\mathbf{V}_0$,

$$n_0(\widetilde{\mathbf{E}} + \widetilde{\mathbf{V}} \times \mathbf{B}_0) + \widetilde{n}\mathbf{V}_0 \times \mathbf{B}_0 - \tau\nabla\widetilde{p}_i = 0, \tag{11}$$

where

$$\mathbf{V}_0 = \frac{\tau}{\rho_0 \mathbf{B}_0^2} \mathbf{B}_0 \times \nabla p_{0i}, \quad \tau = \frac{1}{e_i R_M}\sqrt{\frac{M_i}{\mu_0 n_{0i}}} = \frac{1}{\omega_{Bi}\tau_A}. \tag{12}$$

Here $\widetilde{\mathbf{E}}$ is the perpendicular perturbed electric field, p_{0i} and $\widetilde{p}_i$ are the equilibrium and perturbed ion pressures, ρ_0 is the equilibrium mass density, e_i is the ion charge, n_{0i} is the ion density on axis, $\tau_A \equiv R_0/V_A(0)$, $V_A(0) = B_0(0)/\sqrt{\mu_0\rho_0(0)}$ is the Alfvén velocity on the magnetic axis. For a given pressure profile, all the nonideal MHD terms are proportional to the dimensionless parameter τ, the inverse of the normalized ion-cyclotron frequency ω_{Bi}.

By analogy with Ref. 11, we take into account the term with $\mathbf{V}_0$ in the continuity equation

$$\lambda\widetilde{n} = -\nabla \cdot (n_0\widetilde{\mathbf{V}} + \widetilde{n}\mathbf{V}_0). \tag{13}$$

The perturbed ion temperature $\widetilde{T}_i$ is governed by the ion energy equation allowing for the drift part of the heat flux $\mathbf{q}_i$,

$$\lambda n_0\widetilde{T}_i = -n_0\widetilde{\mathbf{V}} \cdot \nabla T_{0i} - (\Gamma_i - 1)p_{0i}\nabla \cdot \widetilde{\mathbf{V}} - \mathbf{V}_0 \cdot \nabla\widetilde{T}_i$$
$$- (\Gamma_i - 1)\nabla \cdot \widetilde{\mathbf{q}}_i, \tag{14}$$

where

$$\nabla \cdot \widetilde{\mathbf{q}}_i = \tau\frac{\Gamma_i}{(\Gamma_i - 1)}\nabla \cdot \left(\frac{\widetilde{n}T_{0i} + n_0\widetilde{T}_i}{\mathbf{B}_0^2}\mathbf{B}_0 \times \nabla T_{0i} \right.$$
$$\left. + \frac{n_0 T_{0i}}{\mathbf{B}_0^2}\mathbf{B}_0 \times \nabla\widetilde{T}_i \right), \tag{15}$$

T_{0i} is the equilibrium ion temperature, Γ_i is the adiabatic exponent.

The electron energy equation is written in the approximation of infinite parallel electron heat conductivity

$$\mathbf{B}_0 \cdot \nabla\widetilde{T}_e + \widetilde{\mathbf{B}} \cdot \nabla T_{0e} = 0, \tag{16}$$

where $\widetilde{T}_e$ and T_{0e} are the perturbed and equilibrium electron temperature.

B. Transformations of starting equations

We obtain from (11),

$$\widetilde{\mathbf{V}}_\perp = \widetilde{\mathbf{V}}_E - \frac{\widetilde{n}}{n_0}\mathbf{V}_0 + \frac{\tau}{n_0\mathbf{B}_0^2}\mathbf{B}_0 \times \nabla\widetilde{p}_i, \tag{17}$$

where the subscript $\perp$ denotes the vector components perpendicular to the equilibrium magnetic field $\mathbf{B}_0$ and $\widetilde{\mathbf{V}}_E$ is the perturbed cross-field velocity, given by

$$\widetilde{\mathbf{V}}_E = \frac{\widetilde{\mathbf{E}} \times \mathbf{B}_0}{\mathbf{B}_0^2}. \tag{18}$$

Assuming the plasma motion due to the cross-field velocity to be incompressible,

$$\nabla \cdot \widetilde{\mathbf{V}}_E \cong 0, \tag{19}$$

and neglecting the magnetic field curvature effects, one obtains using (15) and (17),

$$\nabla \cdot \widetilde{\mathbf{V}} = \frac{\tau}{n_0\mathbf{B}_0^2}\mathbf{B}_0 \cdot (\nabla n_0 \times \nabla\widetilde{T}_i + \nabla\widetilde{n} \times \nabla T_{0i}), \tag{20}$$

$$(\Gamma_i - 1)\nabla \cdot \widetilde{\mathbf{q}}_i = -\Gamma_i p_{0i}\nabla \cdot \widetilde{\mathbf{V}}. \tag{21}$$

Then (13) and (14) reduce to

$$\lambda\widetilde{n} = -\widetilde{\mathbf{V}}_E \cdot \nabla n_0, \tag{22}$$

$$\lambda\widetilde{T}_i = -\widetilde{\mathbf{V}}_E \cdot \nabla T_{0i}. \tag{23}$$

We then express the electric field by analogy with Ref. 12 as

$$\widetilde{\mathbf{E}} = -\lambda\widetilde{\mathbf{A}}, \tag{24}$$

where $\widetilde{\mathbf{A}}$ is a perturbed vector potential. We use the coordinate system (s, ϑ, ϕ) described in Ref. 1 (s is the dimensionless radial coordinate marking the magnetic surfaces, ϑ is the poloidal coordinate, ϕ is the toroidal angle). Then we obtain from (18),

Phys. Plasmas, Vol. 8, No. 10, October 2001

Modeling of diamagnetic stabilization . . .   4295

$$\lambda A_1 = \hat{V}_E^2, \tag{25}$$

$$\lambda \hat{A}_2 = -V_E^1, \tag{26}$$

where

$$\hat{V}_E^2 = [\widetilde{\mathbf{V}}_E \times \mathbf{B}_0]_1, \quad \hat{A}_2 = [\widetilde{\mathbf{A}} \times \mathbf{B}_0]^1 / \mathbf{B}_0^2. \tag{27}$$

The subscript and superscript 1 denote the first (i.e., sth) covariant and contravariant components, respectively. Substituting Eq. (26) into (22) and (23), we find

$$\tilde{n} = n_0' \hat{A}_2, \quad \tilde{T}_i = T_{0i}' \hat{A}_2, \tag{28}$$

where the prime denotes the derivative with respect to s.

We neglect the parallel perturbed electric field, so that in accordance with (18),

$$\widetilde{\mathbf{A}} \cdot \mathbf{B}_0 = 0. \tag{29}$$

Then, according to Ref. 1,

$$\widetilde{B}^1 = -\mathbf{B}_0 \cdot \nabla \hat{A}_2. \tag{30}$$

Substituting (30) into (16), we find that

$$\widetilde{T}_e = T_{0e}' \hat{A}_2. \tag{31}$$

It follows from (28) and (31) that

$$\tilde{p} = p_0' \hat{A}_2, \tag{32}$$

where $p_0 = n_0 (T_{0i} + T_{0e})$.

Taking into account (17) and (31), the momentum equation (9) can be written in the form

$$\lambda \rho_0 \left\{ \widetilde{\mathbf{V}}_E + \frac{\tau}{\mathbf{B}_0^2} \mathbf{B}_0 \times \nabla \left(\frac{\hat{A}_2 p_{0i}'}{n_0} \right) \right\} = -\nabla(p_0' \hat{A}_2) + \widetilde{\mathbf{H}}. \tag{33}$$

Using (26), we express $\lambda \hat{A}_2$ in terms of V_E^1 and move the relevant term from the left-hand side of (33) to right-hand side of (33). Then the (s, ϑ)-covariant projections of the resulting equation lead to the following equations:

$$\lambda \rho_0 \left(g_{11} V_E^1 + \frac{g_{12}}{fq} \hat{V}_E^2 \right)$$
$$= \hat{\alpha}_1 - \frac{F}{R^2} \frac{\partial}{\partial s} \left\{ G \left[\frac{\partial}{\partial s} (fq \hat{A}_2) - \frac{\partial A_1}{\partial \vartheta} \right] \right\}$$
$$+ \rho_0 \frac{\tau}{fq} \left[-g_{11} \frac{p_{0i}'}{n_0} \frac{\partial V_E^1}{\partial \vartheta} + g_{12} \frac{\partial}{\partial s} \left(\frac{V_E^1 p_{0i}'}{n_0} \right) \right], \tag{34}$$

$$\lambda \rho_0 \left(g_{12} V_E^1 + \frac{g_{22}}{fq} \hat{V}_E^2 \right)$$
$$= \hat{\alpha}_2 - \frac{F}{R^2} G \frac{\partial}{\partial \vartheta} \left[\frac{\partial}{\partial s} (fq \hat{A}_2) - \frac{\partial A_1}{\partial \vartheta} \right]$$
$$+ \rho_0 \frac{\tau}{fq} \left[-g_{12} \frac{p_{0i}'}{n_0} \frac{\partial V_E^1}{\partial \vartheta} + g_{22} \frac{\partial}{\partial s} \left(\frac{V_E^1 p_{0i}'}{n_0} \right) \right]. \tag{35}$$

The functions $\hat{\alpha}_1$, $\hat{\alpha}_2$ were introduced in Ref. 1 as follows:

$$\hat{\alpha}_1 = J(j_0^2 \widetilde{B}^3 - j_0^3 \widetilde{B}^2) - \frac{F}{qR^2} \frac{\partial}{\partial s} [J(M\widetilde{B}^1 + N\widetilde{B}^2)]$$
$$+ \frac{F}{qR^2} \left(\frac{\partial}{\partial \vartheta} + q \frac{\partial}{\partial \phi} \right) [J(L\widetilde{B}^1 + M\widetilde{B}^2)], \tag{36}$$

$$\hat{\alpha}_2 = Jj_0^3 \widetilde{B}^1 + \frac{F}{R^2} \frac{\partial}{\partial \phi} [J(M\widetilde{B}^1 + N\widetilde{B}^2)]. \tag{37}$$

The coefficients L, M, N, G are defined by

$$L = g_{11}/J, \; M = g_{12}/J, \; N = g_{22}/J, \; G = g_{33}/J = F/fq, \tag{38}$$

where the Jacobian $J = fqR^2/F$, $f = 2s\psi_1$ (ψ_1 is the poloidal flux at the boundary), $F = RB_0$ and g_{ik} with $(i,k) = (1,2,3)$ are the metric tensor components. The perturbed magnetic field components $\widetilde{B}^2$ and $\widetilde{B}^3$ are related to A_1, $\hat{A}_2$ by (cf. Ref. 1)

$$\widetilde{B}^2 = \frac{1}{J} \left[\frac{\partial A_1}{\partial \phi} + \frac{\partial}{\partial s} (f\hat{A}_2) \right], \quad \widetilde{B}^3 = \frac{1}{J} \left[\frac{\partial}{\partial s} (fq\hat{A}_2) - \frac{\partial A_1}{\partial \vartheta} \right]. \tag{39}$$

Thus, our model consists of the four equations (25), (26), (34), and (35) for the variables A_1, $\hat{A}_2$, V_E^1, V_E^2. These equations differ from those used in MISHKA-1[1] by the last terms in the square brackets in the right-hand side of (34) and (35).

III. NUMERICAL METHOD

In the numerical scheme, we introduce new variables

$$X_1 = fq\widetilde{V}^1, \quad X_2 = i\hat{V}^2, \quad X_3 = iA_1, \quad X_4 = fq\hat{A}_2 \tag{40}$$

and solve (34), (35), (25), and (26) in their weak form by using the Galerkin method.[12] The four unknown functions are Fourier expanded in both toroidal and poloidal angle; the structure of the functions in radial coordinate s is described in cubic Hermite and quadratic finite elements $H(s)$, i.e., the same discretization as used in the Complex Alfvén Spectrum in TORoidal geometry code (CASTOR[12]) is employed,

$$\widetilde{A} = e^{\lambda t} e^{in\phi} \sum_{m=-\infty}^{+\infty} e^{im\vartheta} \sum_{v=1}^{N} (\widetilde{A}_m)_v H_v(s), \tag{41}$$

where $\widetilde{A}$ is any function from the four functions above. Following the approach described in Ref. 12 we generate the weak forms by multiplying Eqs. (34), (35), (25), and (26) by $(\widetilde{V}^1)^*$, $(\hat{V}^2)^*/fq$, A_1^* and $\hat{A}_2^*$ correspondingly and integrating over the volume $J \, ds \, d\vartheta \, d\phi$. The weak forms are obtained then as follows:

$$\lambda N_1 = M_1 + \tau D_1, \quad \lambda N_2 = M_2 + \tau D_2, \tag{42}$$

$$\lambda N_3 = M_3, \quad \lambda N_4 = M_4, \tag{43}$$

where τ is the dimensionless parameter, which characterizes the ion drift effect and is determined by (12). M_1, M_2 are the parts of weak forms related to the potential energy of the mode,

$$M_1 = \int A(1,3)X_1^*X_3 + A(1',3)\frac{\partial X_1^*}{\partial s}X_3 + A(1,4)X_1^*X_4$$

$$+ A(1',4)\frac{\partial X_1^*}{\partial s}X_4 + A(1,4')X_1^*\frac{\partial X_4}{\partial s}$$

$$+ A(1',4')\frac{\partial X_1^*}{\partial s}\frac{\partial X_4}{\partial s}\,ds\,d\vartheta, \tag{44}$$

$$M_2 = \int A(2,3)X_2^*X_3 + A(2,4)X_2^*X_4$$

$$+ A(2,4')X_2^*\frac{\partial X_4}{\partial s}\,ds\,d\vartheta, \tag{45}$$

the weak forms N_1, N_2 correspond to the kinetic energy,

$$N_1 = \int (B(1,1)|X_1|^2 + B(1,2)X_1^*X_2)ds\,d\vartheta, \tag{46}$$

$$N_2 = \int (B(2,1)X_2^* + B(2,2)|X|^2)ds\,d\vartheta. \tag{47}$$

The weak forms N_3, N_4 and M_3, M_4 connect the vector potential with the plasma velocity,

$$N_3 = \int B(3,3)|X_3|^2 ds\,d\vartheta, \quad N_4 = \int B(4,4)|X_4|^2 ds\,d\vartheta, \tag{48}$$

$$M_3 = \int A(3,2)X_3^*X_2\,ds\,d\vartheta,$$

$$M_4 = \int A(4,1)X_4^*X_1\,ds\,d\vartheta. \tag{49}$$

Similar types of the weak forms were obtained in the MISHKA-1 code, with the only difference that (25) and (26) were used in order to reduce the number of variables from four to two. In contast to the MISHKA-1 code, new terms D_1, D_2 corresponding to the drift effects appear now in the MISHKA-D code:

$$D_1 = \int \left[A(1,1)|X_1|^2 + A(1,1')X_1^*\frac{\partial X_1}{\partial s} \right]ds\,d\vartheta, \tag{50}$$

$$D_2 = \int \left[A(2,1)X_2^*X_1 + A(2,1')X_2^*\frac{\partial X_1}{\partial s} \right]ds\,d\vartheta. \tag{51}$$

The matrix elements [the coefficients in front of the quadratic combinations of the variables X_i ($i=1,2,3$) and their radial derivatives in Eqs. (42)–(51) have to be computed from an equilibrium code (we use the equilibrium code HELENA[13])] by a mapping procedure. Details of the derivation and transformation of the matrix elements are explained in the Appendix.

IV. BENCHMARK OF THE DIAMAGNETIC STABILIZATION OF THE INTERNAL KINK MODE: AUXILIARY MODIFIED VERSIONS OF THE MISHKA-D CODE

Analytic theory for MHD modes in the regime with $|\gamma| \cong \omega_{*i}$ shows that the ω_{*i} stabilization manifests itself in the form of two modes with real frequencies, instead of the modes with imaginary frequencies $\omega = \pm i\gamma_{\text{MHD}}$. Frequencies ω_1 and ω_2 of ω_{*i} stabilized modes are given by

$$\omega_{1,2} = \frac{\omega_{*i}}{2} \pm \sqrt{\frac{\omega_{*i}}{4} - \gamma_{\text{MHD}}^2}. \tag{52}$$

It is seen from (52) that unstable modes with $\text{Im}(\omega) > 0$ can only occur if the value of γ_{MHD} associated with the potential energy of the perturbations becomes high enough to satisfy $\gamma_{\text{MHD}} > \omega_{*i}/2$. Until then only two stable modes can exist with frequencies, which start from $\omega_1 \approx \omega_{*i}$, $\omega_2 \approx \gamma_{\text{MHD}}^2/\omega_{*i}$ at small γ_{MHD} and merge at $\omega_1 \approx \omega_2 \approx \omega_{*i}/2$ as γ_{MHD} increases.

A. The benchmark

As a benchmark case for the MISHKA-D code, the stabilization of the $n=1$ internal kink mode due to the ion-diamagnetic drift is analyzed. Analytically, the growth rate and frequency of the internal kink mode as a function of ω_{*i}, are described by (52). In order to test the MISHKA-D code, the eigenvalues of the internal kink mode are calculated self-consistently, varying the diamagnetic frequency through the parameter τ introduced in (52), keeping the pressure profile constant. The equilibrium used is characterized by the pressure and current profiles: $p' = p'(0)(1 - \psi)$ and $\langle j \rangle = j(0)(1 - \psi)$, where ψ is a normalized poloidal flux. A circular plasma boundary is chosen, with the aspect ratio of $R_0/a = 4$. The poloidal beta and the safety factor on-axis values are, correspondingly, $\beta_p \equiv 8\pi S\langle p \rangle/\mu_0 I^2 = 0.4$ and $q(0) = 0.75$. This equilibrium is unstable with respect to the ideal MHD $n=1$ internal kink mode.[10] Here, $\langle p \rangle$ is the volume averaged pressure, S the area of the poloidal cross section of the plasma, and I the total toroidal plasma current. The trajectory of the growth rate, $\gamma = \text{Re}(\lambda)$, and the frequency, $\omega = \text{Im}(\lambda)$ of the two modes as a function of τ is shown in Fig. 1. The behavior of the two modes is in good agreement with (52). At $\tau = 0$, one unstable and a stable, damped, mode exist, both with the same mode structure. With increasing τ, the frequency of the two modes increases linearly with ω_{*i}, while the growth and damping rates are decreasing. At $\omega = \omega_{*i}/2$ the two modes coalesce. Further increase in ω_{*i} leads to two stable modes, one increasing, the other decreasing in frequency. The value of ω_{*i} as evaluated at the $q=1$ surface from a toroidal analogue of (1):

$$\omega_{*i} = \tau \frac{nq\langle|\nabla\psi|\rangle}{\rho_0\langle r\rangle\langle B_0\rangle}\frac{dp}{d\psi}, \tag{53}$$

agrees within 5% with the value of ω_{*i} determined from the linear increase of $\text{Im}(\lambda)$ with τ (the brackets $\langle\cdots\rangle$ denote an averaging over the flux surface).

The variation of ω_{*i} with τ corresponds to a variation of the plasma density or magnetic field, which leaves the (normalized) equilibrium and thus the pressure unchanged. Varying the total pressure changes both the ideal MHD growth rate of the mode and the diamagnetic frequency. Figure 1(b) shows the frequency and growth rate as a function of the poloidal beta for both ideal and finite ω_{*i}. The ideal MHD internal kink mode is stable up to a poloidal beta of β_p
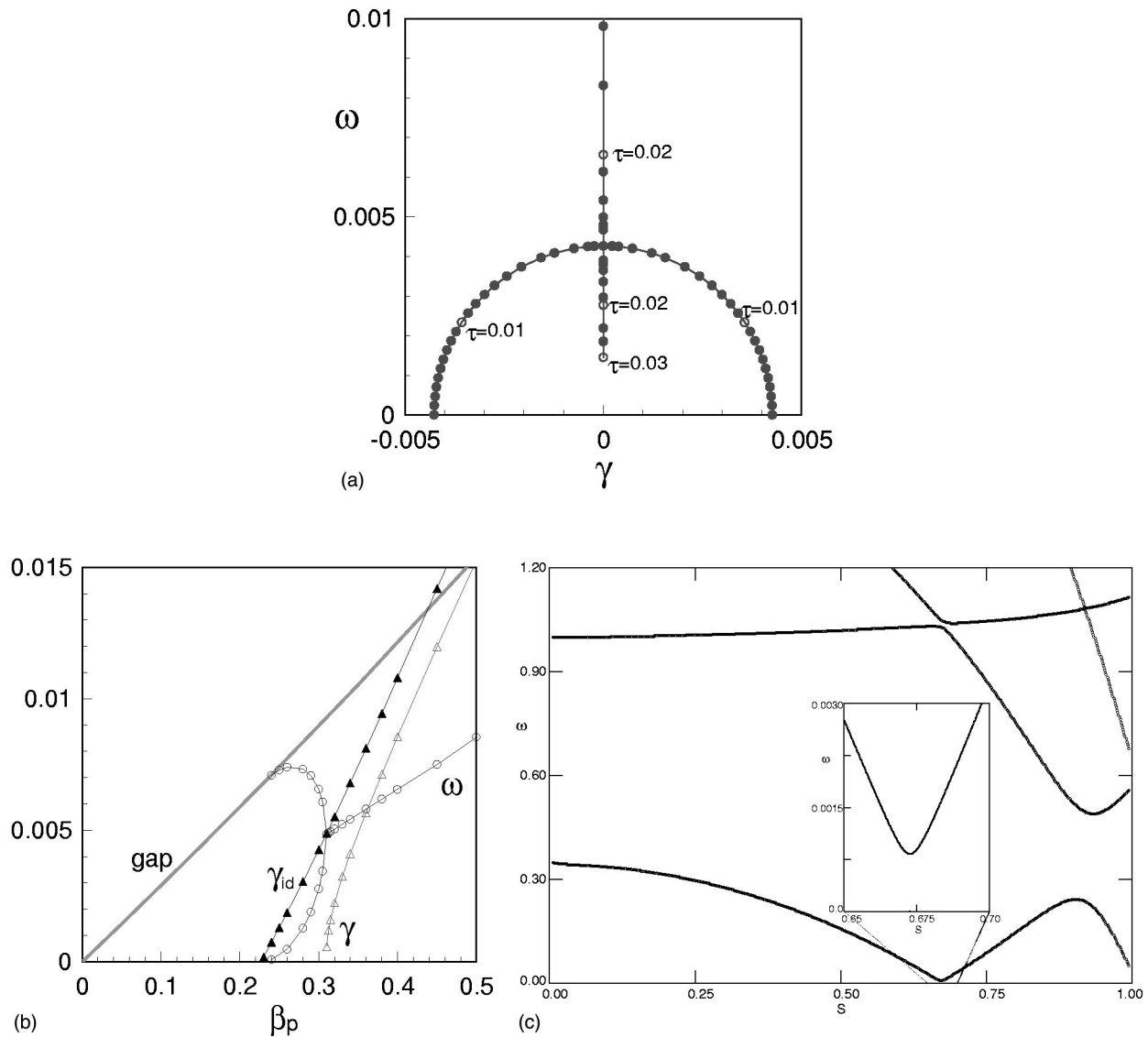
Phys. Plasmas, Vol. 8, No. 10, October 2001

Modeling of diamagnetic stabilization . . . 4297

FIG. 1. (a) The trajectory of the growth rate, γ, and the frequency, ω of the $n=1$ internal kink mode as a function of ω_{*i}. (b) Growth rate (γ, open triangles) and frequency (ω, circles) of the internal kink mode as a function of the poloidal beta at fixed $\tau=0.02$. The ideal MHD growth rate, γ_{id}, is given by the filled triangles. The frequency at the top off the ω_{*i} induced gap is also shown. (c) The radial structure of the Alfvén continuum modified by ω_{*i} as a function of the radial coordinate $s=\sqrt{\psi/\psi_1}$. The $n=1$ internal kink mode with eigenvalues shown in (b) has its frequency at the bottom of the gap induced by ω_{*i}.

$=0.226$. The effect of ion-diamagnetic drift ($\tau=0.02$) gives rise to two stable modes. However, the two stable modes only exist when the pressure is larger than the ideal MHD stability limit.

B. Auxiliary version of the MISHKA-D code for computing the Alfvén continuum

For lower values of the pressure the frequencies of the stable modes would lie inside the Alfvén continuum. The diamagnetic drift frequency modifies the Alfvén continuum in the low-frequency range by inducing "gaps" in the continuum at the intersection points between branches of oscillations $\omega=\pm k_{\|m}(r)V_A(r)$ and $\omega=\omega_{*i}(r)$.[14] The finite ω_{*i} induces a gap in the continua of width from $\omega=0$ to $\omega=\omega_{*i}$. In order to compute the continuum frequencies with ω_{*i} effect for shaped equilibrium with arbitrary radial profiles of density, pressure and $q(r)$, a modified version of the

MISHKA-D code, similar to the CSCAS code,[15] was developed. The bottom of the gap as a function of β_p computed by the modified MISHKA-D is shown in Fig. 1(b). The radial structure of the continuum modified by ω_{*i} is shown in Fig. 1(c). At the marginally stable value of the pressure of the ideal mode, one global mode comes out of the continuum with a frequency $\omega=\omega_{*i}$, the second mode comes out of the continuum below the ω_{*i} induced gap at $\omega=0$. With increasing pressure, the two modes coalesce when $\gamma=\omega_{*i}/2$ and the internal kink becomes unstable (at $\beta_p=0.308$).

C. The antenna version of the MISHKA-D code

In order to study global eigenmodes of finite frequency, which can be excited by external antenna, the antenna MISHKA-D code was developed similar to Refs. 16 and 17. This auxiliary version of the MISHKA-D code allows computing the plasma response to the wave field of the external
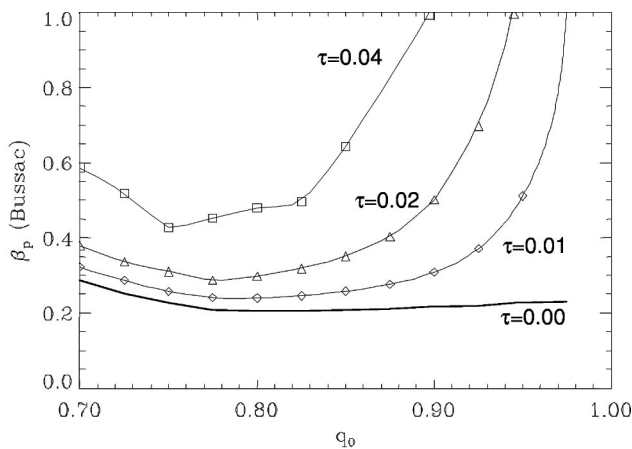
FIG. 2. Stability limits of $n=1$ internal kink mode modified due to diamagnetic stabilization as a function of $\tau = 1/(\omega_{Bi}\tau_A)$.

antenna. When the external antenna drives a wave field with certain m,n and the driving frequency is swept across the frequency range of interest, sharp resonances are detected in the plasma response at frequencies, which correspond to the frequencies of global eigenmodes of the same helicity.

It is known that, experimentally, the frequency of the two stable modes can be determined by exciting the modes with an external antenna.[18] Using the separation of the frequencies of the two stable modes in (52) as an indication of the distance to the stability limit of the mode, one could, in principle, avoid MHD instabilities through a feedback system to control the plasma parameters. However, the two stable modes can only be observed when they are ideally unstable, but ω_{*i} stabilized. Below the ideal MHD stability limit the two modes become continuum modes and cannot be detected as individual modes by an external excitation with an antenna. This point has been verified with the antenna version of the MISHKA-D code. When the global modes exist, sharp resonances are found in the plasma response to the external drive from the antenna. However, as soon as the frequency of the global modes fall inside the continuum, the sharp resonances are lost and only the response from the continuum remains. Thus, the interval of plasma parameters where the stable modes can be detected entirely depends on the effectiveness of the diamagnetic stabilization.

In order to investigate the efficiency of the ω_{*i} stabilization of the internal kink, the marginally stable values of the poloidal beta have been computed with the MISHKA-D code as a function of q on axis, for four values of the parameter τ. The value of the safety factor on-axis, $q(0)$, is varied by changing the total current, at fixed equilibrium profiles. Figure 2 shows the resulting stability limits of the internal kink, estimated from (52) for $\tau = 0$, 0.01, 0.02, and 0.04. The ideal MHD limit is in good agreement with the classical result for the Bussac mode.[10] The ideal MHD growth rate scales with the square of the inverse aspect ratio of the $q=1$ surface, i.e., the growth rates become very small as $q(0)$ approaches 1. With the choice of the shape of the pressure profile, ω_{*i} is almost constant as a function of radius. The stabilizing effect of the ion-diamagnetic drift is therefore largest for small radii of the $q=1$ surface (see Fig. 2).

V. STABILITY OF IDEAL MHD MODES IN THE *H*-MODE EDGE TRANSPORT BARRIER

The pressure gradient in the transport barrier at the edge of an *H*-mode plasma is limited by MHD instabilities in the form of edge localized modes (ELMs). The relevant instabilities are ballooning modes driven by the edge pressure gradient and localized kink (peeling) modes driven by the edge current, which is due to both the bootstrap current and the Ohmic current related to the high edge electron temperature. Usually, experiments show that the pressure gradient in the *H*-mode edge pedestal is found to correspond to the first ballooning stability limit[6,19] and it follows the scaling with α ($\alpha = -4(q^2/\varepsilon B_0^2)V^{1/2}(dp/dV)$) as expected for the ballooning limit. Under some conditions, e.g., at high shaping and/or high $q(95)$, the pressure gradient is found to be significantly above the first ballooning stability limit.[20,21] This may be explained by the access to the second zone of the ballooning stability, which is most easily achieved at high triangularity and high $q(95)$ (high poloidal beta). An alternative explanation for the pressure gradients exceeding the ideal MHD first ballooning stability limit is the stabilizing influence of the ion-diamagnetic drift velocity.[7,8] In Ref. 7, the influence of the diamagnetic drift was analyzed using the Braginskii equations in a flux tube geometry with a shifted circle equilibrium. In the following section, the influence of the diamagnetic drift on the finite-*n* ballooning stability and kink/peeling modes in the edge pedestal is analyzed in full toroidal geometry, using the linearized MHD equations as described above. Finally, in order to quantify the importance of the stabilizing influence of the diamagnetic drift, the stability limits of a JET hot-ion *H*-mode discharge are determined as functions of ω_{*i}.

A. Finite-*n* ideal ballooning modes in the edge pedestal

In ideal MHD, the stability limit of ballooning modes with $n=\infty$ has been adopted in order to interpret the stability of edge pressure gradients in tokamaks. In this approach, the marginally stable pressure gradient does not depend on the width of the edge pedestal, and the width of the mode is assumed to be infinitely small. However, physically relevant instabilities have finite mode numbers and for finite-*n* ballooning modes with a finite mode width, the width of the edge pedestal is an important parameter in the stability limits.[22]

In order to clarify the influence of the pedestal width on the stability of ideal MHD finite-*n* ballooning modes, we computed with the MISHKA-1 code the marginally stable pressure gradients and the growth rates as functions of the toroidal mode number and the width of the edge pedestal. The formulation of the MHD equations in the MISHKA codes and the accuracy of the higher order finite elements used in both the equilibrium (HELENA[11]) and in the stability calculations allow toroidal mode numbers up to $n<100$ to be analyzed in full toroidal geometry.

The equilibrium used is characterized by a circular plasma boundary, an inverse aspect ratio $R_0/a=4$, q at the boundary just below 4 and the poloidal beta of 1.0. The edge
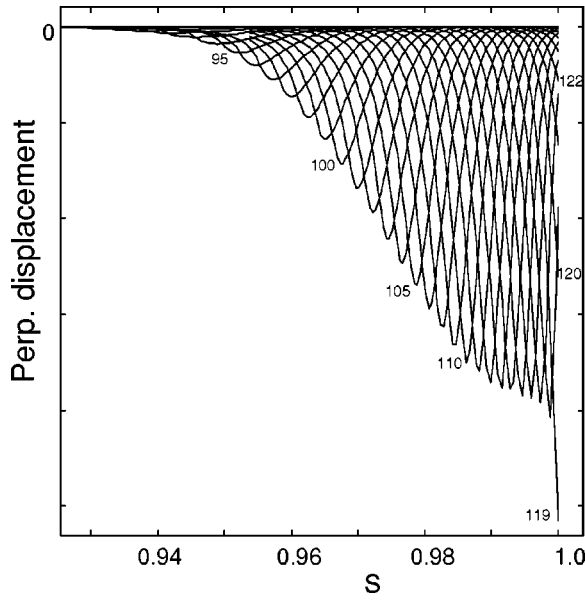
FIG. 3. Radial mode structure (poloidal harmonics) of $n=30$ ideal MHD unstable edge ballooning mode. The pedestal extends from $s=0.95$ to $s=1$.

FIG. 5. (a) The growth rates of the ballooning modes as a function of the pressure gradient, $\alpha(98)$, for the toroidal mode numbers varying in the range $10<n<40$. (b) Variation of the growth rates as a function of the pressure gradient for different values of the safety factor q at the edge, $\Delta=n(q_1-q_{\text{int}})=0.1$ (circles), 0.5 (triangles), 0.9 (diamonds).

pedestal is represented by a local gradient, which is added to the pressure profile: $p'(\psi)=1-\psi+p_1[(\psi-\psi_b)^2(3-2\psi-\psi_b)/(1-\psi_b)^3]^{1/4}$. The increased pressure gradient (with amplitude p_1) extends from ψ_b to the boundary, $\psi=1$. The flux surface average current density profile is given by $\langle j \rangle =1-0.8\psi-0.2\psi^2$. In the stability calculations an ideally conducting wall is positioned at twice the minor radius.

Assuming that (52) can be used for approximately estimating the influence of the diamagnetic drift frequency for ballooning modes, we first study stability of the ideal MHD finite-n ballooning modes in the edge pedestal with the use of the MISHKA-1 ideal MHD code. Figure 3 shows the typical finite-n ballooning mode with toroidal mode number $n=30$ in the edge transport barrier.

Figure 4 shows the marginally stable pressure gradient, α_c, as a function of the toroidal mode number for three values of the width of the pedestal. The value of the marginally stable pressure gradient can be well described by

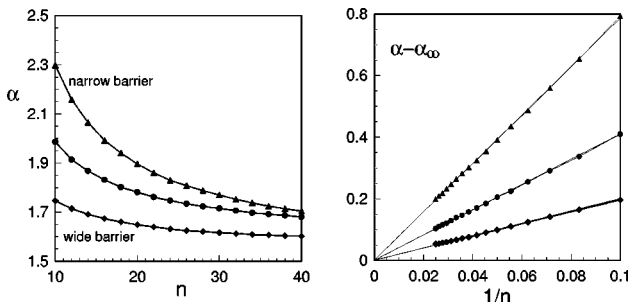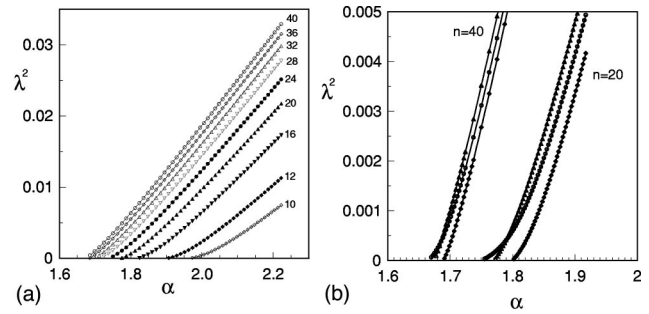$$\alpha_c(n)=\alpha_\infty+c_\alpha/(\delta_b n), \qquad (54)$$

FIG. 4. The marginally stable critical pressure gradient, α_c, as a function of the toroidal mode number n for three different values of the width of the edge pedestal, $\delta_b=0.025$, 0.05, and 0.10. On the right, $\alpha(n)-\alpha\ (n=\infty)$ as a function of n^{-1} shows a linear scaling.

where δ_b is the width of the transport barrier, $\delta_b=(1-\psi^{1/2})$, and α_∞ is an extrapolated value to $n=\infty$.

In (54), the $1/n$ correction of the marginal α is consistent with the conventional ballooning theory. It does not follow the modified scaling with $n^{-2/3}$ for the edge ballooning mode,[22] since the $n^{-2/3}$ scaling is related to a linear variation of the growth rate of the $n=\infty$ ballooning mode. However, for the pressure gradient profile in the barrier used in our analysis here, the $n=\infty$ growth rate varies quadratically as a function of ψ (as in the conventional ballooning theory), with a maximum just inside the plasma boundary. In order to obtain a linear variation of the $n=\infty$ growth rate the pressure gradient has to increase faster than the magnetic shear. It is also seen from (54), that the correction to α_c is inversely proportional to the width of the edge pedestal, and narrow barriers are more stable with respect to finite-n ballooning modes, than wide barriers.

The width (as measured by the half-width of the envelope of the ballooning mode at the outboard mid-plane) of the computed eigenfunction of the ballooning mode in the edge pedestal, shown in Fig. 3, shows a strong scaling with the pedestal width and a weak dependence on the toroidal mode number. The half-width can be approximated by $\delta_{\text{HW}}\cong\delta_b^{3/4}n^{-1/4}$, and it does not follow the $n^{-1/2}$ dependence typical of the conventional ballooning theory, or the edge ballooning mode scaling $n^{-2/3}$.[22] The number of rational surfaces inside the half-width of the mode increases linearly with the toroidal mode number as opposed to the $n^{1/2}$ scaling from the ballooning theory. This measure of the mode width in terms of the number of rational surfaces gives a mode width independent of toroidal mode number. The width of the ballooning mode basically fills up the width of the pedestal.

In the presence of the finite diamagnetic drift frequency, Eq. (52) shows that the increase in the marginal pressure gradient due to the diamagnetic stabilization is determined by the change in the growth rate of the ideal MHD mode with α relative to the change in ω_{*i} with α. The growth rates $\text{Re}(\lambda)$ of the ideal MHD finite-n ballooning for $\delta_b=0.05$, are shown in Fig. 5 as a function of the edge pressure gradient for several values of the toroidal mode number. The variation of the growth rate versus pressure gradient relative

to the variation of the diamagnetic frequency determines the amplitude of the diamagnetic stabilization. Close to marginal stability, for the range of toroidal mode numbers considered ($10<n<40$), the growth rates of the ideal MHD high-n modes can be approximated by

$$\lambda^2 = c_2 n(\alpha - \alpha_c), \tag{55}$$

where constant c_2 does not depend on the pedestal width. For larger growth rates, $\lambda>0.05$, the growth rate is found to follow the scaling

$$\lambda^2 = c_0(1 - c_1/n)(\alpha - \alpha_c). \tag{56}$$

[The α_c values in (55) and (56) have slightly different numerical values.] The constant c_0 is independent of the pedestal width, whereas c_1 shows a weak inverse dependence on δ_b. The scaling of the growth rate close to marginal stability in (56) is due to the free boundary contribution to the instability, and it strongly depends on the value of q at the boundary. However, the slope $\lambda^2(\alpha)$ for larger growth rates away from marginal stability is independent of q at the boundary. This is illustrated in Fig. 5(b), which shows the growth rates for several values of q at the boundary. In computing Fig. 5, it was important to keep the parameter $\Delta = n(q_1 - q_{int})$ (Ref. 22) constant (q_1 is the value of q at the boundary and q_{int} is the integer value nearest to q_1), in order to keep the free boundary contribution constant as a function of the mode number. Since the ideal growth rates close to the marginal stability are easily stabilized by the diamagnetic drift, the behavior at large growth rates is more relevant for the stability limit in the presence of diamagnetic stabilization.

B. Diamagnetic stabilization of edge ballooning modes

We now use the MISHKA-D code in order to compute diamagnetic drift effect on the edge ballooning modes. Since the diamagnetic frequency increases linearly with the toroidal mode number, $\omega_{*i} = c_\omega n\alpha\tau$, and the growth rate of the edge ballooning mode saturates with increasing n, a critical value for n should exist, above which the ballooning modes are stable when diamagnetic stabilization is taken into account. This is illustrated in Fig. 6, which shows the contours of the marginally stable values of the pressure gradient based on the scaling of the ideal MHD growth rate as a function of the toroidal mode number and the parameter τ. The maximum of each contour of α, as indicated in Fig. 6, corresponds to the most unstable mode number n. With increasing value of τ, and increasing ω_{*i}, the toroidal mode number of the most unstable mode rapidly decreases. An expansion in τ and $1/n$ of (55), yields for the dependence of the most unstable mode number, for small values of τ:

$$n_{max} = \left(\frac{2c_0 c_\alpha}{\alpha_\infty^2 c_\omega^2}\right)^{1/3} \tau^{-2/3}, \quad \alpha(n) = \alpha_\infty + \frac{3}{2}\frac{c_\alpha}{n_{max}}. \tag{57}$$

For a large enough value of τ, the higher-n modes become unconditionally stable for any value of the pressure gradient. Above a critical τ (~0.028 in this case), all finite-n ballooning modes are stable. This situation is similar to the so-called second stable regime for $n=\infty$ ballooning modes where this regime can be obtained through shaping of the plasma
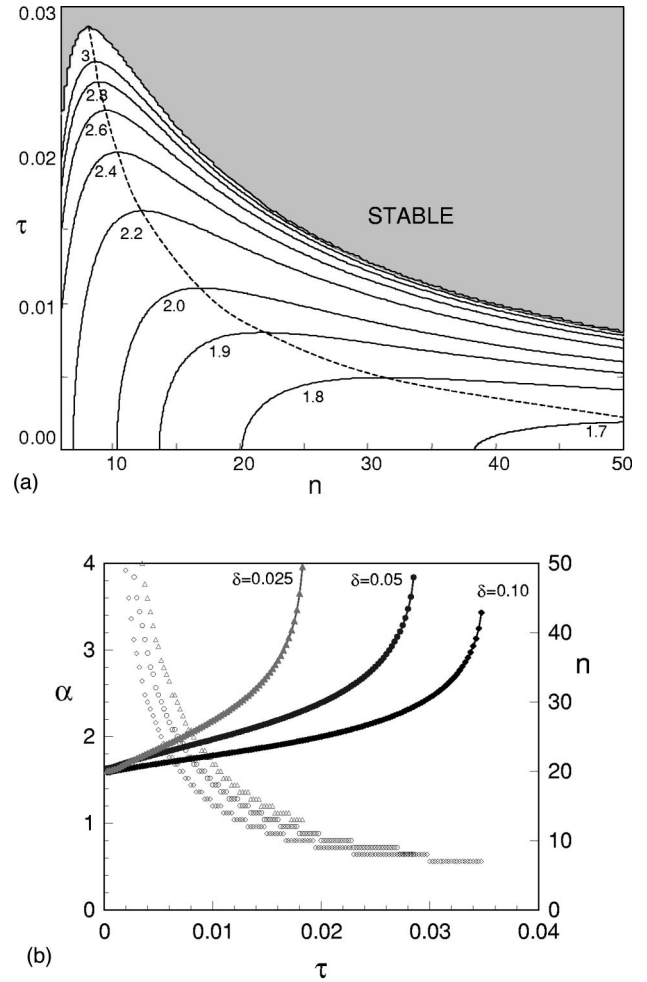

FIG. 6. (a) Contours of the marginally stable values of the pressure gradient, $\alpha(98)$, as a function of the toroidal mode number, n, and parameter τ for the edge pedestal of width $\delta_b=0.05$. The dashed line indicates the most unstable toroidal mode number at each value of τ. (b) Marginally stable pressure gradients $\alpha(98)$ and the most unstable toroidal mode numbers n as functions of $\tau=1/(\omega_{Bi}\tau_A)$ for three different values of the width of the pedestal, $\delta_b=0.025$ (triangles), 0.05 (circles), 0.10 (diamonds), based on the computed ideal MHD growth rates.

boundary and/or at high poloidal beta. Figure 6(b) shows the influence of the width of the edge pedestal on the ballooning stability including the diamagnetic stabilization. Since the lower-n mode numbers are more stable at smaller widths of the pedestal, in accordance with (54), the influence of the diamagnetic stabilization is more important for small pedestal widths. The change in the marginally stable pressure gradient scales approximately with the pedestal width. Thus, the increase of the pressure due to the diamagnetic stabilization at the top of the pedestal is independent of the width of the pedestal. However, the access to the second stable regime, which can be induced by ω_{*i}, does depend on the pedestal width; a wide pedestal requires a larger value for τ.

After the discussion of the influence of the diamagnetic stabilization based on the ideal MHD growth rates and simple analytical expression (52), we compare our main conclusions with the numerical calculation of the stability limits with the MISHKA-D code. The computed behavior of the growth rate and frequency of an $n=30$ ballooning mode with
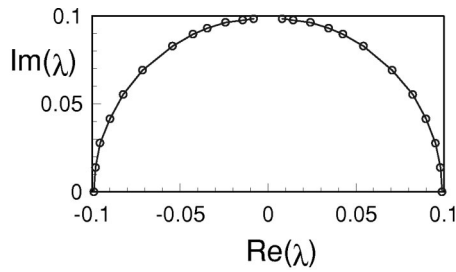
FIG. 7. The growth/damping rate and the frequency of $n=30$ ballooning mode as functions of the ion-diamagnetic frequency, ω_{*i}, at constant pressure gradient, computed with the MISHKA-D code. (τ varies from 0 to 0.006.)

FIG. 9. The kink and ballooning stability limits as functions of the edge pressure gradient and the normalized edge current density, J_1/J_0, for $\tau=0$ (thin lines) and $\tau=0.02$ (fat lines). Here J_1 is the edge current density, J_0 is the volume-averaged toroidal current density. Included also is the ideal MHD ballooning limit for $n=\infty$ (dashed). The shaded areas are stable.

increasing ω_{*i} is shown in Fig. 7. For the chosen shape of the edge transport barrier, the eigenvalue of the ballooning mode follows (52) closely, showing a good correlation between the simplified formula (52) and the computed eigenvalues. The marginally stable values for the pressure gradient as a function of the toroidal mode number, as calculated with the MISHKA-D code, are plotted in Fig. 8 for several values of τ. The resulting marginally stable values for α agree very well with the values based on the ideal MHD growth rates for $\tau<0.02$. For $\tau=0.01$, the most unstable mode is $n=20$ and no stability limit is found for modes with toroidal mode numbers larger than 40. For $\tau=0.02$, the stabilization is somewhat less effective than in (52), due to the increased interaction with the Alfvén continuum. Although the eigenfrequency of the marginally stable mode computed at $\tau=0.02$ falls inside the gap induced by the diamagnetic effects in the edge pedestal, it falls inside the first Alfvén gap outside the edge pedestal. This causes a significant change in the mode structure, which extends well beyond the edge pedestal in this case.

C. Low-n kink (peeling) and ballooning modes

In addition to the medium to high-n pressure driven ballooning modes, the MHD stability of the H-mode edge pedestal is determined by low- to medium-n kink modes. The kink modes (also called peeling modes) are driven unstable by the edge current density, which consists mostly of boot-
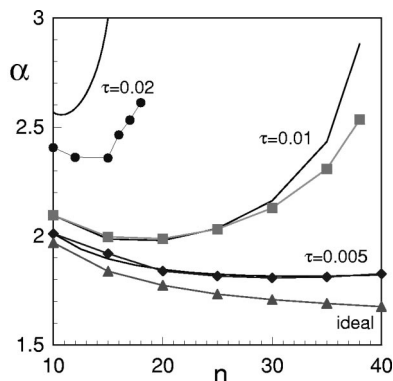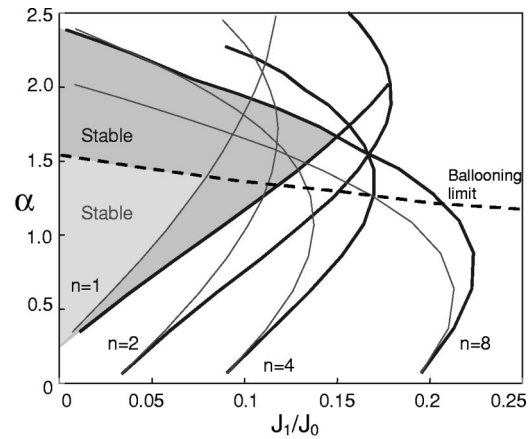

FIG. 8. Marginally stable values of the pressure gradient $\alpha(98)$ in the pedestal for different values of the parameter τ computed with the MISHKA-D code (symbols). The lines indicate relevant marginally stable values estimated from the ideal MHD growth rates.

strap current due to the edge pressure gradient. Even in ideal MHD the edge pressure gradient is known to have a significant stabilizing effect on the kink modes, for pressure gradients below the ballooning limit.[23] This stabilizing effect is largest for the lower-n kink modes. When the edge pressure gradient is of the order of the ballooning limit, the medium-n kink modes are destabilized by the pressure gradient. In this regime, the instability is a combination of a kink and a ballooning mode. The ideal MHD stability limits due to the $n=1$, 2, 4, and 8 modes as a function of both the edge pressure gradient and the edge current density are shown in Fig. 9. The equilibrium is the same model equilibrium as used in Figs. 3–8. To calculate the stability limits, the pressure gradient and the current density inside the edge pedestal have been varied independently. For each toroidal mode number more than 600 equilibria have been analyzed. With the choice of q at the boundary just below 4, the $n=1$ kink mode is the most unstable mode at low pressure gradients. In ideal MHD without diamagnetic stabilization, the stable operating space is limited by the $n=1$ mode in the direction of the edge current density and by the $n\rightarrow\infty$ ballooning mode in the direction of the edge pressure gradient.

The low-n stability limits including the ion-diamagnetic drift ($\tau=0.02$), as computed with the MISHKA-D code, are also shown in the edge stability diagram, Fig. 9. Comparison with the ideal MHD stability limits clearly shows the additional stabilizing effect of the pressure due to the diamagnetic drift. At pressure gradients close to the ideal ballooning limit the stabilizing effect of the diamagnetic drift on the low-n kink modes is of the same order for the different mode numbers. This is because both the growth rate and the diamagnetic frequency increase linearly with mode number.

The stable space with the diamagnetic drift included is still limited by the $n=1$ kink mode in the direction of the edge current density but the highest stable edge current is almost a factor of 2 higher. At this point, the stability limits of $n=1$, 2, 4, and 8 modes are very similar. The pressure gradient is now limited by the $n=8$ mode but at a value
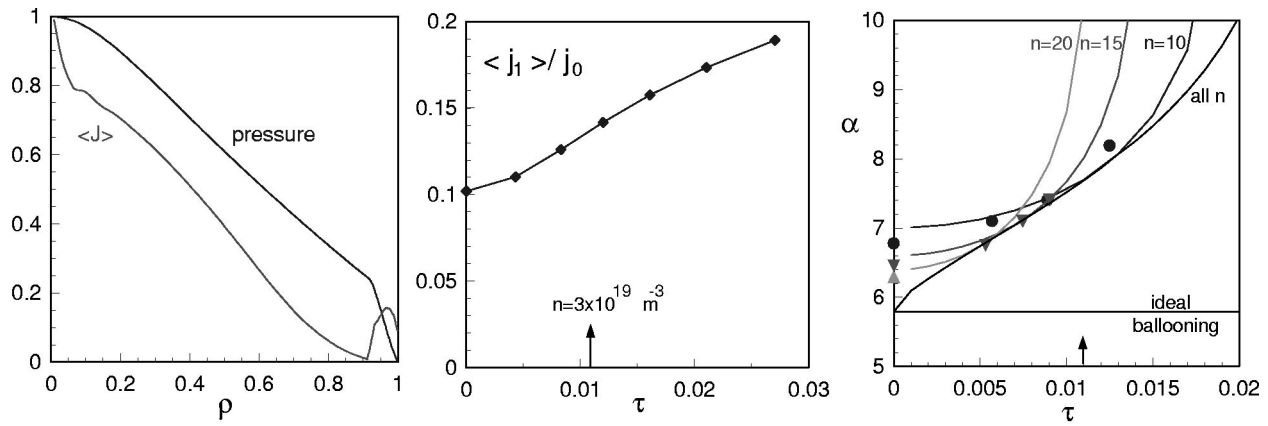
FIG. 10. The $n=2$ external kink limit (center) and the finite-n ballooning mode limit (right) as functions of τ for JET hot-ion H-mode discharge #42677. The marginally stable pressure gradients, computed with the MISHKA-D code, are indicated by symbols, while the lines show the relevant values based on the ideal MHD growth rates. On the left, the equilibrium profiles of the pressure and the toroidal current density as functions of the normalized radius are shown.

significantly above the ideal MHD ballooning limit.

(For this circular equilibrium the second stable regime for ideal ballooning modes exists only for $j_1/j_0 > 0.42$ and is not accessible due to the low-n stability limits.)

D. Stability of the edge barriers in JET hot-ion *H*-mode

In order to quantify the importance of the ω_{*i} stabilization for typical tokamak parameters, the stability limits due to kink and ballooning modes have been calculated for the edge barrier of JET hot-ion H-mode DT discharge (pulse #42677[4]) at the time of maximum fusion performance. The pressure profile and the current density profile are taken from transport simulation of this discharge with the JETTO code.[24] Figure 10 shows the typical large edge pressure gradient and the local increase in the edge current density. The width of the edge transport barrier is about 4 cm. The relevant stability limits for this discharge are plotted in Fig. 10 as a function of τ. The maximum edge current density is limited by $n=2$ kink (peeling) mode, localized inside the edge pedestal. The increase in the marginally stable edge current due to the diamagnetic stabilization is found to be to first order linear in τ, due to the linear dependence of the growth rate on the edge current density. At a density of $n=3\times10^{19}$ m^{-3} and the relevant parameter $\tau=0.011$, the marginally stable value of the edge current density is increased by 35% as compared to the ideal MHD limit. At $\tau=0.011$, the critical pressure gradient is limited by an $n=10$–15 ballooning mode at a pressure gradient which is about 30% higher than the $n=\infty$ ideal MHD ballooning limit. For the ballooning limit, for each individual toroidal mode number, the increase of the marginally stable pressure gradient scales quadratically in τ for small values of τ. However, considering all toroidal mode numbers gives a more linear dependence because the most unstable mode number goes down with increasing τ (see Fig. 10). Thus, both the kink and ballooning limits in the edge pedestal have significant dependence on the density due to stabilization by the ion-diamagnetic drift, being more stable at low density.

VI. STABILITY LIMIT IN SHEAR-OPTIMIZED SCENARIOS

The main MHD limitation in shear-optimized scenarios is due to the ideal MHD $n=1$ global pressure driven mode, described in detail in Ref. 3. For this mode, the effect of radial variation of the diamagnetic drift frequency ω_{*i} is very important, due to the global character of the mode eigenfunction, and very sharp pressure gradients.

For typical plasma profiles in JET shear-optimized scenario (pulse #40572), the eigenvalue and the mode structure computed by the MISHKA-D code is shown in Fig. 11. The behavior of this mode as a function of τ does not follow the simple dispersion relation (52). The mode is not completely stabilized for any value of τ and the frequency of the mode has a maximum as a function of τ, see Fig. 11(a). This behavior is related to the large variation of ω_{*i} at the different rational surfaces, due to the large pressure gradients at or inside the transport barrier. One consequence is that the marginally stable mode has no frequency. Complete stabilization could, in principle, be obtained when the density profile balances the radial change in the pressure gradient such that ω_{*i} is relatively constant as a function of radius. However, using the estimate typical of the ideal MHD growth rates, $\lambda^2 \propto (\beta_p - \beta_{pm})$, the increase in the marginally stable beta would scale only quadratically with τ. Thus, the influence on the ion drift velocity on the $n=1$ stability limit in shear-optimized discharges is very small, in spite of the large value of the ion diamagnetic frequency ω_{*i} calculated locally at the foot of the internal transport barrier. This is consistent with the good agreement between the calculated ideal MHD stability limits and the observed disruptive stability limit in the shear-optimized scenarios, previously analyzed in Ref. 3.

VII. CONCLUSIONS

Equations have been derived which extend the one-fluid ideal MHD model to include the effect of the ion-diamagnetic drift, which is important for typical plasma parameters in the transport barriers. These equations have been implemented as an extension of the ideal MHD code
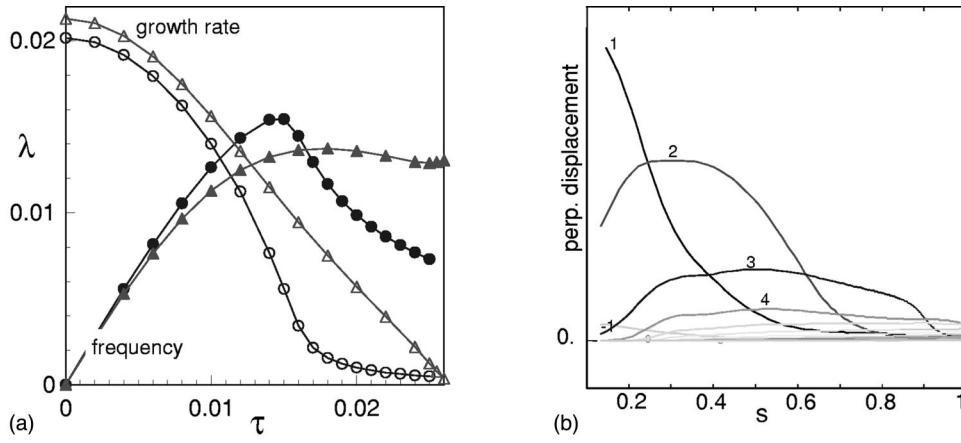
FIG. 11. (a) Growth rates (open symbols) and frequencies of the global pressure driven kink mode in equilibrium computed for JET shear-optimized scenario (pulse #40572) as functions of the parameter τ (circles). Included is also a case with a small radial variation of the diamagnetic frequency (triangles). (b) Radial structure of the poloidal harmonics of the radial displacement of the global pressure driven $n=1$ mode.

MISHKA-1.[1] The new MISHKA-D code allows us to perform an accurate self-consistent computation of both stable and unstable eigenmodes with eigenvalues $|\gamma| \cong \omega_{*i}$ up to a very large toroidal mode number ($n < 50–100$) in full toroidal geometry. The ω_{*i} spectrum of the $n=1$ internal kink eigenmodes computed as a benchmark of the MISHKA-D code shows a good agreement with the analytic theory. In order to perform a comprehensive analysis of the ω_{*i} spectrum and to compute the plasma response to the drive from external antenna, two auxiliary versions of the MISHKA-D code were also developed, the continuum solver similar to CSCAS code,[15] and the antenna MISHKA-D code similar to Refs. 16 and 17.

The MISHKA-D code has been used to analyze the stabilizing influence of ω_{*i} effect on the stability limits of finite-n ballooning and low-n kink (peeling) modes in the transport barriers of H-mode discharges. Both the kink and ballooning modes show a significant stabilization due to the ion-diamagnetic drift. For a given pressure profile, the amplitude of the ion-diamagnetic drift terms is proportional to the parameter τ, the ion-cyclotron frequency normalized to the Alfvén frequency. Since this parameter scales with the major radius and density as $R_0^{-1} n_{0i}^{-1/2}$, the effect is strongest at low plasma densities in smaller tokamaks. Consequently, the edge stability limits depend on the density, being more stable at low density. For the specific JET hot-ion H-mode discharge analyzed, at the density of the edge pedestal 3 $\times 10^{19}$ m^{-3}, an increase of about 30% in the plasma pressure threshold was found for both the ballooning and kink modes due to the ion diamagnetic drift effect. Due to the scaling of the growth rate of the finite-n ballooning modes with the width of the edge pedestal, the stabilizing effect is found to be largest for small pedestal widths.

By including the diamagnetic drift in the stability calculations of the finite-n ideal ballooning modes, the highest n modes (which are the most unstable modes in ideal MHD) are stabilized first. The most unstable ballooning mode is found to be a medium-n mode whose exact mode number depends on the parameter τ determined by the density in the edge transport barrier. For large enough values of τ a second stability zone is obtained where the finite-n ballooning modes are stable for any value of the mode number n and pressure gradient. The numerical analysis has shown, that the radial structure of the finite-n ballooning mode in the edge pedestal differs from what one would expect from the conventional ballooning theory (or the modified theory for the plasma edge[22]). The width of the mode depends mostly on the width of the high pressure gradient region in the edge pedestal, and the mode fills the whole width of the pedestal. The mode width depends only weakly on the toroidal mode number. Usually, the effect of an unstable ballooning mode is assumed to be benign, leading to a soft limit to the pressure gradient. This scenario is based on considering the $n \to \infty$ ideal ballooning modes and taking into account their strong localization. However, considering the finite-n ideal ballooning modes at finite ω_{*i}, a medium-n ballooning mode with a mode width of the order of the edge pedestal is found to be the most unstable, and at a crossing of the ballooning limit this mode may well lead to a discrete ELM event.

For JET optimized shear discharges with internal transport barrier, the ω_{*i} effect on the disruptive $n=1$ global pressure driven kink mode is found to be weak, due to the effect of radial variation of the ion diamagnetic frequency ω_{*i}. This result is in agreement with the good correlation between the observed stability limits due to disruptions and the calculated ideal MHD stability limits.[3]

ACKNOWLEDGMENTS

APPENDIX: DERIVATION AND TRANSFORMATION OF THE MATRIX ELEMENTS

In order to illustrate the procedure of obtaining the matrix elements we consider the quadratic form (42). We start from the expression

$$N_1 = \int \rho_0 \frac{R^2}{fqF^2}(g_{11}X_1 - ig_{12}X_2)X_1^* \, ds \, d\vartheta. \quad (A1)$$

Comparison of (A1) and (46) gives the matrix elements

$$B(1,1) = \rho_0 \frac{R^2 g_{11}}{fqF}, \quad B(1,2) = -i\rho_0 \frac{R^2 g_{12}}{fqF}. \quad (A2)$$

4304   Phys. Plasmas, Vol. 8, No. 10, October 2001

Huysmans *et al.*

The metric tensor components g_{ik} can be obtained from the known expressions for the associated metric tensor components g^{ik}:

$$g^{11}=|\nabla s|^2, \quad g^{12}=g^{21}=\nabla s \cdot \nabla \vartheta$$
$$g^{22}=|\nabla \vartheta|^2, \quad g^{33}=1/R^2. \tag{A3}$$

Taking into account the relation

$$g_{ik}=(-1)^{i+k}M^{ik}/J^2, \tag{A4}$$

where M^{ik} is the minor of g^{ik}, we obtain

$$g_{11}=\frac{J^2}{R^2}|\nabla \vartheta|^2, \quad g_{12}=g_{21}=-\frac{J^2}{R^2}\nabla s \cdot \nabla \vartheta,$$
$$g_{22}=\frac{J^2}{R^2}|\nabla s|^2, \quad g_{33}=R^2. \tag{A5}$$

Since the equilibrium code HELENA does not directly compute the function $|\nabla \vartheta|^2$, we express this function by using the condition

$$J^2=|g_{ik}|\equiv(g_{11}g_{22}-g_{12}^2)R^2, \tag{A6}$$

where $|g_{ik}|$ is the determinant of the metric tensor. Then we obtain

$$g_{11}=\frac{1}{|\nabla s|^2}+\frac{J^2}{R^2}\cdot\frac{(\nabla s \cdot \nabla \vartheta)^2}{|\nabla s|^2}. \tag{A7}$$

In addition, since the HELENA code computes $\nabla \psi$, we use the relation

$$\nabla s=\nabla \psi/f, \tag{A8}$$

in order to obtain ∇s. As a result, we transform the matrix components g_{ik} ($i,k=1,2$) to

$$g_{11}=\frac{f^2}{|\nabla \psi|^2}+\frac{f^2 q^2 R^2}{F^2}\cdot\frac{(\nabla \psi \cdot \nabla \vartheta)^2}{|\nabla \psi|^2}, \tag{A9a}$$

$$g_{12}=g_{21}=-\frac{fq^2R^2}{F^2}\nabla \psi \cdot \nabla \vartheta, \tag{A9b}$$

$$g_{22}=\frac{q^2R^2}{F^2}|\nabla \psi|^2. \tag{A9c}$$

Then (A2) reduces to

$$B(1,1)=\rho_0\frac{fR^2}{qF}\left[\frac{1}{|\nabla \psi|^2}+\frac{q^2R^2}{F^2}\cdot\frac{(\nabla \psi \cdot \nabla \vartheta)^2}{|\nabla \psi|^2}\right], \tag{A10a}$$

$$B(1,2)=i\rho_0\frac{qR^4}{F^3}\nabla \psi \cdot \nabla \vartheta. \tag{A10b}$$

Similarly, one obtains the remaining elements of the B matrix:

$$B(2,1)=-B(1,2), \tag{A11a}$$

$$B(2,2)=\frac{\rho_0 qR^4}{fF^3}|\nabla \psi|^2, \tag{A11b}$$

$$B(3,3)=B(4,4)=1. \tag{A11c}$$

The matrix elements on the right-hand side of (44) are

$$A(1,3)=-\frac{in}{F}\cdot(2\bar{m}-m+nq)(\nabla \psi \cdot \nabla \vartheta)+\frac{n}{fqF^2}\left(q\frac{dF}{ds}\right.$$
$$\left.-2F\frac{dq}{ds}\right)|\nabla \psi|^2-\frac{n}{fF}\cdot\frac{\partial|\nabla \psi|^2}{\partial s}+\frac{m}{fq}\cdot\frac{dF}{ds}, \tag{A12a}$$

$$A(1',3)=\frac{n}{fF}|\nabla \psi|^2-\frac{mF}{fq}, \tag{A12b}$$

$$A(1,4)=\frac{1}{fq^3F^2}\frac{dq}{ds}\left(2F\frac{dq}{ds}-q\frac{dF}{ds}\right)|\nabla \psi|^2$$
$$+2i\frac{\bar{m}-m}{Fq^2}\frac{dq}{ds}\nabla \psi \cdot \nabla \vartheta+\frac{f}{Fq}(m+nq)$$
$$\times(\bar{m}+nq)\left[\frac{(\nabla \psi \cdot \nabla \vartheta)^2}{|\nabla \psi|^2}+\frac{F^2}{q^2}\cdot\frac{1}{R^2|\nabla \psi|^2}\right]$$
$$+\frac{1}{fq^2F}\frac{dq}{ds}\frac{\partial}{\partial s}|\nabla \psi|^2, \tag{A12c}$$

$$A(1',4)=i\frac{m+nq}{Fq}\nabla \psi \cdot \nabla \vartheta-\frac{1}{fq^2F}\frac{dq}{ds}|\nabla \psi|^2, \tag{A12d}$$

$$A(1,4')=-i\frac{2\bar{m}-m+nq}{Fq}\nabla \psi \cdot \nabla \vartheta-\frac{1}{fq^2F^2}\left[2F\frac{dq}{ds}\right.$$
$$\left.-q\frac{dF}{ds}\right]|\nabla \psi|^2-\frac{1}{fqF}\frac{\partial}{\partial s}|\nabla \psi|^2-\frac{1}{fq}\frac{dF}{ds}, \tag{A12e}$$

$$A(1',4')=\frac{1}{fqF}(F^2+|\nabla \psi|^2). \tag{A12f}$$

Somewhat simpler matrix elements are obtained for the right-hand sides of (45) and (49):

$$A(2,3)=-\frac{1}{fqF}(m^2F^2+n^2q^2|\nabla \psi|^2), \tag{A13a}$$

$$A(2,4)=-i\frac{1}{Fq}(m+nq)(m-\bar{m}+nq)\nabla \psi \cdot \nabla \vartheta$$
$$+\left[(m+2nq)\frac{1}{fq^2F}\frac{dq}{ds}-\frac{1}{fqF^2}(m+nq)\frac{dF}{ds}\right]$$
$$\times|\nabla \psi|^2+\frac{m+nq}{fqF}\frac{\partial}{\partial s}|\nabla \psi|^2, \tag{A13b}$$

$$A(2,4')=\frac{1}{fqF}(mF^2-nq|\nabla \psi|^2), \tag{A13c}$$

$$A(3,2)=1, \tag{A13d}$$

$$A(4,1)=-F-\frac{|\nabla \psi|^2}{f}. \tag{A13e}$$

The ''drift'' matrix elements [see (50) and (51)] in terms of g_{ik} are given by

Phys. Plasmas, Vol. 8, No. 10, October 2001

Modeling of diamagnetic stabilization . . .   4305

$$A(1,1) = \rho_0 \frac{R^2}{Ffq} \left[-i \frac{m}{fq} \cdot \frac{p'_{0i}}{n_0} g_{11} + g_{12} \frac{\partial}{\partial s} \left(\frac{p'_{0i}}{fqn_0} \right) \right],$$

(A14a)

$$A(1,1') = \rho_0 \frac{R^2}{Ff^2q^2} \cdot \frac{p'_{0i}}{n_0} g_{12},$$

(A14b)

$$A(2,1) = \rho_0 \frac{fqR^2}{F} \left[g_{12} \frac{m}{fq} \cdot \frac{p'_{0i}}{n_0} + i g_{22} \frac{\partial}{\partial s} \left(\frac{p'_{0i}}{fqn_0} \right) \right],$$

(A14c)

$$A(2,1') = i\rho_0 \frac{R^2}{F} \cdot \frac{p'_{0i}}{n_0} g_{22}.$$

(A14d)

We substitute (A9) in (A14) and obtain

$$A(1,1) = \rho_0 \frac{R^2}{F} \left[-im \frac{p'_{0i}}{q^2 n_0} \cdot \left[\frac{1}{|\nabla \Psi^2|} + \frac{q^2 R^2}{F^2} \right. \right.$$
$$\left. \left. \cdot \frac{(\nabla \psi \cdot \nabla \vartheta)^2}{|\nabla \psi|^2} \right] - \frac{qR^2}{F^2} \cdot \frac{\partial}{\partial s} \left(\frac{p'_{0i}}{fqn_0} \right) \cdot (\nabla \psi \cdot \nabla \vartheta) \right],$$

(A15a)

$$A(1,1') = -\rho_0 \frac{R^4}{fF^3} \cdot \frac{p'_{0i}}{n_0} (\nabla \psi \cdot \nabla \vartheta),$$

(A15b)

$$A(2,1) = \frac{\rho_0 f q^2 R^4}{F^3} \left[-m \frac{p'_{0i}}{n_0} (\nabla \psi \cdot \nabla \vartheta) \right.$$
$$\left. + i q |\nabla \psi|^2 \frac{\partial}{\partial s} \left(\frac{p'_{0i}}{fqn_0} \right) \right],$$

(A15c)

$$A(2,1') = i\rho_0 \frac{p'_{0i}}{n_0} \cdot \frac{R^4 q^2 |\nabla \psi|^2}{F^3}.$$

(A15d)

[1] A. B. Mikhailovskii, G. T. A. Huysmans, S. E. Sharapov, and W. Kerner, Plasma Phys. Rep. **23**, 844 (1997).

[2] G. T. A. Huysmans, T. Hender, and B. Alper, Nucl. Fusion **38**, 179 (1998).

[3] G. T. A. Huysmans, T. Hender, B. Alper *et al.*, Nucl. Fusion **39**, 1489 (1999).

[4] M. Keilhacker, A. Gibson, C. Gormezano *et al.*, Nucl. Fusion **39**, 209 (1999).

[5] C. Gormezano, Y. F. Baranov, C. D. Challis *et al.*, Phys. Rev. Lett. **80**, 5544 (1998).

[6] J. W. Connor, R. J. Hastie, H. R. Wilson, and R. L. Miller, Phys. Plasmas **5**, 2687 (1998).

[7] B. N. Rogers and J. F. Drake, Phys. Plasmas **6**, 2797 (1999).

[8] R. J. Hastie, P. J. Catto, and J. J. Ramos, Phys. Plasmas **7**, 4561 (2000).

[9] A. B. Mikhailovskii, *Instabilities in a Confined Plasma* (IOP, Bristol, 1998).

[10] M. N. Bussac, R. Pellat, D. Edery, and J. L. Soule, Phys. Rev. Lett. **35**, 1638 (1975).

[11] A. B. Mikhailovskii, Plasma Phys. Controlled Fusion **40**, 1907 (1998).

[12] W. Kerner, J. P. Goedbloed, G. T. A. Huysmans, S. Poedts, and E. Schwartz, J. Comput. Phys. **142**, 271 (1998).

[13] G. T. A. Huysmans, J. P. Goedbloed, and W. Kerner, *Proceedings of the CP90 Conference on Computer Physics* (World Scientific, Singapore, 1991), p. 371.

[14] A. B. MIkhailovskii, *Reviews of Plasma Physics* (Consultants Bureau, New York, 1967), Vol. 3, p. 159.

[15] S. Poedts and E. Schwartz, J. Comput. Phys. **105**, 165 (1993).

[16] G. T. A. Huysmans, W. Kerner, D. Borba, H. A. Holties, and J. P. Goedbloed, Phys. Plasmas **2**, 1605 (1995).

[17] H. A. Holties, A. Fasoli, J. P. Goedbloed, G. T. A. Huysmans, and W. Kerner, Phys. Plasmas **4**, 709 (1997).

[18] A. Fasoli, J. B. Lister, S. E. Sharapov *et al.*, Nucl. Fusion **35**, 1485 (1995).

[19] P. Gohill, M. Ali Mahdavi, L. Lao *et al.*, Phys. Rev. Lett. **61**, 1603 (1988).

[20] H. Zohm, Plasma Phys. Controlled Fusion **38**, 105 (1996).

[21] L. Lao, J. R. Ferron, R. L. Miller *et al.*, Nucl. Fusion **39**, 1785 (1999).

[22] J. W. Connor, Plasma Phys. Controlled Fusion **40**, 531 (1998).

[23] G. T. A. Huysmans, C. D. Challis, M. Erba, W. Kerner, and V. V. Parail, *Proceedings of the 22nd European Physical Society Conference on Controlled Fusion and Plasma Physics, Bournemouth, 1995* (European Physical Society, Petit-Lancy, 1995), Vol. 19C, I-201.

[24] A. Cherubini, M. Erba, V. Parail, E. Springmann, and A. Taroni, Plasma Phys. Controlled Fusion **38**, 1421 (1996).

[25] P. H. Rebut and the JET Team, *Plasma Physics and Controlled Nuclear Fusion Research, 1984, Proceedings of the 10th International Conference, London* (International Atomic Energy Agency, Vienna, 1985), Vol. 1, p. 11.